Chemical Science

ROYAL SOCIETY OF CHEMISTRY

EDGE ARTICLE

View Article Online
View Journal | View Issue

A strategy of chiral cation coordination to achieve a large luminescence dissymmetry factor in 1D hybrid manganese halides†

Fei Wang,[abc] Xingjun Li,*[abc] Tianqi Chen,[abc] Liqing Wang,[ac] Chenliang Li,[ac] Wei Zhang,[ac] Wen Yuan,[abc] Shan Lu,[abc] Lina Li[abc] and Xueyuan Chen[abc]

Check for updates

Cite this: *Chem. Sci.*, 2025, **16**, 11012

All publication charges for this article have been paid for by the Royal Society of Chemistry

Received 28th February 2025
Accepted 13th May 2025

DOI: 10.1039/d5sc01615k

rsc.li/chemical-science

Chiral organic–inorganic metal halides (OIMHs) have emerged as a new class of promising circularly polarized luminescence (CPL) materials owing to their structural tunability and fascinating optoelectronic properties. However, the development of high-performance chiral hybrid OIMHs remains a critical challenge, largely attributed to the absence of effective strategies for modulating chiroptical activity. Herein, we present enantiomeric hybrid manganese bromides, denoted as *R*/*S*-DACAMnBr$_3$, featuring a one-dimensional chain structure alternately coordinated by organic cations *via* edge-sharing MnOBr$_5$ octahedra, which establishes a robust chiral transfer pathway from organic cations to inorganic emissive centers. This structural design synergizes with the high intrinsic emission efficiency of Mn^{2+} centers to achieve intense orange CPL at 626 nm, yielding a remarkable luminescence dissymmetry factor (g_{lum}) of 0.292 for *S*-DACAMnBr$_3$, which surpasses most reported chiral OIHMs by 1–3 orders of magnitude. Remarkably, a positive magneto-chiroptical effect under a 1.6 T magnetic field amplifies the g_{lum} value to 0.321 at room temperature, demonstrating the first example of magnetic-field-enhanced CPL in lead-free OIMHs. The practical viability is further evidenced by *S*-DACAMnBr$_3$-based circularly polarized light-emitting diodes exhibiting a strong CPL signal at 620 nm with a g_{lum} of 6.4×10^{-3}, alongside single-crystal photodetectors achieving a switching ratio of 7.72. These findings contribute valuable insights for amplifying the chiroptical activity of hybrid OIMHs *via* a strategy of chiral cation coordination, which may pave the way for the development of effective CPL materials toward diverse applications in the future.

Introduction

Circularly polarized luminescence (CPL) materials hold immense potential for advancing optoelectronic technologies,[1] such as circularly polarized light-emitting diodes (CP-LEDs),[2–6] three-dimensional (3D) displays, CPL switches, CPL detectors,[7,8] and spintronic devices.[9–11] Conventional CPL systems such as organic small molecules, polymers, and inorganic nanomaterials often face a fundamental trade-off between achieving high luminescence efficiency and large luminescence dissymmetry factors (g_{lum}).[12–15] While liquid crystalline composites demonstrate strong chiroptical activity, their practical deployment is hindered by complex synthetic protocols.[16] In contrast, chiral organic–inorganic metal halides (OIMHs) have emerged as a promising alternative, offering structural versatility, superior optical properties, and scalable fabrication.[17–20] Among these, chiral manganese-based halides stand out due to their exceptional photochemical stability, high photoluminescence quantum yields (PLQY), and low toxicity,[21–24] rendering them as versatile platforms for developing high-performance CPL materials with additional functionalities such as ferroelectricity and magneto-chiroptical coupling.[25–27]

Despite these advantages, reconciling intense emission with large g_{lum} values poses a considerable challenge in chiral OIMHs.[28] Recent strategies to amplify chiroptical activity have focused on modulating inorganic framework distortions *via* weak non-covalent interactions (*e.g.*, hydrogen bonding or halogen–halogen contacts).[29–32] For example, Quan *et al.* proved that solvent-induced lattice distortions in zero-dimensional (0D) $[\mathrm{MnBr_4}]^{2-}$ tetrahedra can elevate g_{lum} from 10^{-4} to 10^{-3}.[33] Similarly, halogenation of chiral cations in layered lead iodides enhanced the rotatory strength of the electronic transition, yielding a g_{lum} of 3.1×10^{-3}.[34] However, such approaches suffer from inefficient chirality transfer from organic ligands to inorganic emitters due to the weak and long-range nature of

---

[a] *State Key Laboratory of Structural Chemistry, Fujian Key Laboratory of Nanomaterials, Fujian Institute of Research on the Structure of Matter, Chinese Academy of Sciences, Fuzhou, Fujian 350002, China. E-mail: lixj@fjirsm.ac.cn*

[b] *College of Chemistry and Materials Science, Fujian Normal University, Fuzhou, Fujian 350117, China*

[c] *Fujian College, University of Chinese Academy of Sciences, Fuzhou, Fujian 350116, China*

† Electronic supplementary information (ESI) available: Experimental details, spectral data and additional data. CCDC 2378510 and 2378511. For ESI and crystallographic data in CIF or other electronic format see DOI: **https://doi.org/10.1039/d5sc01615k**

these interactions. Recent breakthroughs in coordination-driven structural design have addressed this limitation by leveraging stronger covalent coordination bonds. Notably, Mao *et al.* achieved a record g_{lum} of 0.328 in chiral hybrid manganese bromides through direct Mn–O coordination, surpassing hydrogen-bonded analogues by 40 fold.[35] Despite this progress, critical gaps persist, including the limited library of chiral amines capable of forming such coordination architecture, unclear mechanisms of chiral signal amplification, and a lack of practical demonstrations in optoelectronic devices.

In this work, we report enantiomeric hybrid manganese bromides, denoted as *R*/*S*-DACAMnBr$_3$, featuring a one-dimensional (1D) chain structure constructed from edge-sharing MnOBr$_5$ octahedra alternately coordinated by chiral (1*R*, 2*R*)/(1*S*, 2*S*)-2-aminocyclohexanol (DACA) cations. This unique architecture establishes a robust chiral transfer pathway from organic cations to Mn^{2+} emitters, synergizing with the intrinsic high PLQY of Mn^{2+} to achieve intense orange CPL at 626 nm with an exceptional g_{lum} of 0.292, which surpasses most chiral OIMHs by 1–3 orders of magnitude. Furthermore, positive magneto-chiroptical effect under a 1.6 T magnetic field enhances the g_{lum} to 0.321 at room temperature (RT). The practical viability of the obtained chiral OIMHs is illustrated through *R*/*S*-DACAMnBr$_3$-based CP-LEDs and single-crystal photodetectors. This work not only provides an effective strategy for amplifying the chiroptical activity of OIMHs through coordination-driven chirality transfer but also advances the development of versatile CPL materials for next-generation optoelectronics.

Results and discussion

Structural characteristics

Single crystals of the enantiomeric hybrid manganese bromides, *R*/*S*-DACAMnBr$_3$, were synthesized *via* a solution reaction of Mn(CH$_3$COO)$_2$ with chiral (1*R*, 2*R*)/(1*S*, 2*S*)-2-aminocyclohexanol (DACA) in hydrobromic acid. Single-crystal X-ray diffraction analysis confirmed that both compounds crystallize in a non-centrosymmetric orthorhombic system with the chiral space group $P2_12_12_1$, showing identical unit cell parameters (Table S1†). Fig. 1a presents the molecular stacking pattern of the unit cell for *R*-DACAMnBr$_3$, and the asymmetric unit of *R*-DACAMnBr$_3$ comprises one MnBr$_3$ subunit coordinated to a DACA cation. Notably, the structure adopted a 1D chain motif along the *a*-axis, formed by edge-sharing MnOBr$_5$ octahedra alternately coordinated by chiral DACA ligands (Fig. 1b). This alternating coordination mode, previously observed in axial staggered systems,[36] contrasted with conventional chiral OIMHs where organic–inorganic interactions are dominated by weak hydrogen bonding. Here, the Mn^{2+} center was directly bonded to the hydroxyl group of DACA and five bromide ions, forming a distorted MnOBr$_5$ octahedron, which is a structural hallmark critical for efficient chirality transfer. Recent work demonstrated that the lattice distortion induced by the chiral molecules was likely to be the dominant factor for the chirality.[8] The octahedral distortion was quantified by significant variations in bond lengths and angles (Tables S2–S5†). For *R*-DACAMnBr$_3$, Mn–O/Br bond lengths ranged from 2.218 Å to 2.711 Å, while intraoctahedral angles spanned from 84.15° to 176.33°. Similar distortions were observed in *S*-DACAMnBr$_3$ (2.223–2.709 Å, 83.99–176.25°), confirming the structural equivalence of the enantiomers. The pronounced distortion arose from the asymmetric coordination environment imposed by the chiral DACA ligand, which disrupted the octahedral symmetry and induced a helical twist in the 1D chain. This structural asymmetry was further stabilized by multiple hydrogen bonds (O–H···Br, N–H···Br, and C–H···Br; Fig. S1†), ensuring tight integration between organic and inorganic components. The chirality of *R*/*S*-DACAMnBr$_3$ was unequivocally demonstrated by their non-superimposable mirror-image geometries (Fig. 1c and S2†). The alternating coordination architecture established a short-range chiral transfer pathway from the chiral DACA ligand to the Mn^{2+} emitter, circumventing the limitations of long-range non-covalent interactions in conventional systems. This direct coupling mechanism, combined with the high intrinsic luminescence characteristics of Mn^{2+}, is anticipated to synergistically enhance CPL efficiency. The 1D chains showed Mn^{2+}–Mn^{2+} distances from 3.900 Å to 15.769 Å (Fig. S3†), reflecting the periodic arrangement of octahedra along the chain. This structural periodicity, coupled with the chiral distortion, may facilitate the amplification of chiroptical activity in *R*/*S*-DACAMnBr$_3$.

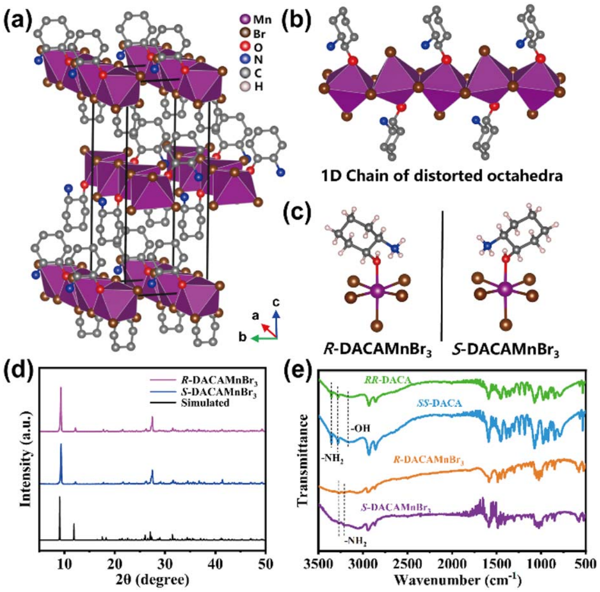

Fig. 1 Structural characterization of *R*/*S*-DACAMnBr$_3$. (a) Single-crystal structure and packing diagram of *R*-DACAMnBr$_3$ (H atoms are omitted for convenience). (b) Infinite 1D chain of MnOBr$_5$ octahedra alternately coordinated by DACA ligands. (c) MnOBr$_5$ octahedra of *R*/*S*-DACAMnBr$_3$ enantiomers showing nonsuperimposable mirror images. (d) Simulated and experimental powder XRD patterns of *R*/*S*-DACAMnBr$_3$. (e) FT-IR spectra of *RR*/*SS*-DACA and *R*/*S*-DACAMnBr$_3$.

X-ray photoelectron spectroscopy (XPS) further confirmed the presence of C, O, N, Br, and Mn elements in *R*-DACAMnBr$_3$ crystals, with the Mn 2p$_{3/2}$ and 2p$_{1/2}$ peaks centered at 641.2 eV and 653.5 eV, respectively, consistent with the +2 oxidation state of Mn^{2+} ion (Fig. S4†). Powder X-ray diffraction (PXRD) patterns of both enantiomers exhibited excellent agreement with simulations derived from single-crystal data (Fig. 1d), confirming their high phase purity and long-range crystallographic order. Fourier-transform infrared (FT-IR) spectroscopy provided additional evidence of the organic–inorganic integration. The disappearance of –OH stretching vibration and a redshift of the $–NH_2$ stretching vibration indicated coordination and hydrogen bonding interactions between the DACA ligands and the Mn^{2+} centers (Fig. 1e).

Photoluminescence properties

The ultraviolet-visible (UV-Vis) absorption spectra of *R*/*S*-$DACAMnBr_3$ crystals revealed a strong absorption band in the ultraviolet (UV) region at 300 nm. This absorption can be attributed to the absorption of the chiral DACA ligand, as illustrated in Fig. 2a and S5.† Additionally, several absorption peaks were identified within the wavelength range of 310 nm to 600 nm. These peaks correspond to the electronic transitions of Mn^{2+} from the ground state $^6A_1(S)$ to the excited states $^4T_1(P)$, $^4E(D)$, $^4T_2(D)$ $^4A_1/^4E(G)$, $^4T_2(G)$, and $^4T_1(G)$, respectively, as reported in ref. 37 As depicted in the insets of Fig. 2b, under ambient light conditions, *R*-$DACAMnBr_3$ crystals demonstrated a light pink and transparent appearance. When irradiated with 365 nm UV light, they displayed bright orange PL emission. Due to the similar chemical components and structural characteristics, both enantiomeric crystals showed a broad orange emission band upon irradiation with 357 nm UV light. This emission band extended from 550 nm to 800 nm, peaking around 626 nm with a full-width at half-maximum (FWHM) of 266 meV (85 nm), and it exhibited a large Stokes shift of 105 nm. A large Stokes shift is beneficial as it helps to mitigate self-absorption, thereby enhancing the emission efficiency. Upon 357 nm excitation, the average PLQY was determined to be 32.2% for *R*-$DACAMnBr_3$, and 18.7% for *S*-$DACAMnBr_3$ (Fig. S6†). The PLE spectra of the crystals displayed a high degree of overlap with the absorption bands of both DACA ligands and Mn^{2+} ions, which indicates an efficient energy transfer process from the chiral organic ligands to the Mn^{2+} centers. Time-resolved PL decay curves for both enantiomers fit well to a single-exponential model, yielding average PL lifetimes of 0.98 ms (*R*) and 0.72 ms (*S*) at 626 nm under ambient excitation conditions (Fig. 2c and S7†). Based on the PL lifetimes and PLQYs, we calculated the non-radiative rate constants (k_{nr}) of *R*/*S*-$DACAMnBr_3$ crystals at RT (Table S6†). The *R*-$DACAMnBr_3$ crystals manifested a smaller k_{nr} value than *S*-$DACAMnBr_3$ ($6.92 \times 10^2\ s^{-1}$ *vs.* $1.13 \times 10^3\ s^{-1}$), demonstrating a reduced non-radiative decay pathway in *R*-$DACAMnBr_3$ crystals, which endowed them with an enhanced PL emission.

To gain deep insights into the origin of the broadband orange emission in *R*/*S*-$DACAMnBr_3$, wavelength-dependent PLE and PL emission spectra were systematically analyzed. As depicted in Fig. 2d and e for *R*-$DACAMnBr_3$, the PL emission maximum at 626 nm and PLE peaks remain invariant across varying wavelengths, confirming the absence of multiple emissive centers. Furthermore, the integrated emission intensity displayed a linear relationship with incident excitation power density, ruling out defect-mediated recombination mechanisms (Fig. S8†).[38] This result combining with the PLE and excitation wavelength-dependent PL spectra unambiguously attributed the broadband emissions of *R*/*S*-$DACAMnBr_3$ crystals to a single Mn^{2+} luminescent center in octahedra from the same excited state, featuring a distinct d–d ($^4T_1(G)$–$^6A_1$) transition.[39] The

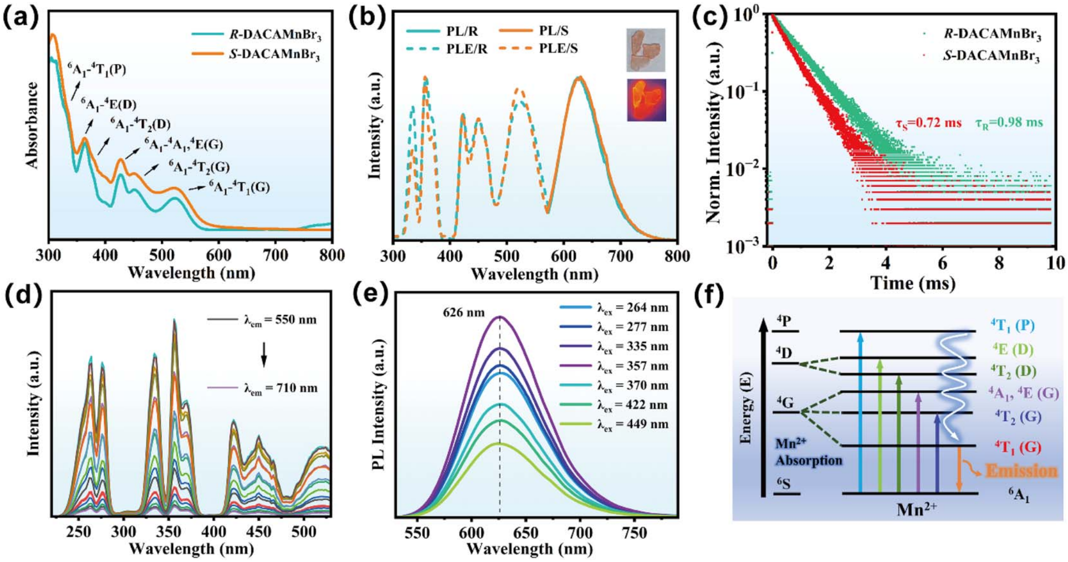

Fig. 2 Photoluminescence properties of *R*/*S*-$DACAMnBr_3$ at RT. (a) UV-vis absorption spectra of *R*/*S*-$DACAMnBr_3$. (b) Steady-state excitation and emission spectra of *R*/*S*-$DACAMnBr_3$. (c) Time-resolved PL decay spectra ($\lambda_{em} = 626$ nm) of *R*/*S*-$DACAMnBr_3$ at RT. (d) Photoluminescence emission (PLE) spectra of *R*-$DACAMnBr_3$ by monitoring the Mn^{2+} emission at different wavelengths. (e) PL spectra of *R*-$DACAMnBr_3$ with different excitation wavelengths. (f) Schematic energy level diagram of the octahedrally coordinated Mn^{2+} ion in *R*-$DACAMnBr_3$ and the energy transfer mechanism for the orange emission at 626 nm.

invariance of spectral features under varying excitation conditions underscored the stability of the Mn^{2+} coordination environment. Fig. 2f illustrates the proposed energy-level diagram for Mn^{2+} in *R*/*S*-DACAMnBr$_3$, comparing the electronic states of free Mn^{2+} ions with those in the distorted $MnOBr_5$ octahedral field.[40] The crystal field splitting induced by the asymmetric coordination lowers the energy of the $^4T_1(G)$ excited state, resulting in the observed orange emission at 626 nm.

To elucidate the excited state dynamics, we conducted temperature-dependent steady-state PL spectroscopic analysis on *R*-DACAMnBr$_3$. Under 357 nm excitation, photophysical properties such as the PL peak position, PL intensity, and FWHM were monitored over a temperature range of 80–300 K. The pseudo-color PL emission spectra showed pronounced temperature-dependent behavior. As temperature decreased from 300 K to 80 K, the excitation and emission intensities of *R*-DACAMnBr$_3$ crystals exhibited a substantial enhancement (Fig. 3a and S9†), which can be attributed to reduced electron–phonon coupling and suppression of non-radiative recombination of Mn^{2+} at cryogenic temperatures.[41,42] Meanwhile, a distinct redshift was observed in the Mn^{2+} emission band, shifting from 626 nm at 300 K to 640 nm at 80 K. This phenomenon can be ascribed to lattice contraction-induced enhancement of d–d splitting in Mn^{2+}, which consequently reduced the energy gap for the $^4T_1 \rightarrow {}^6A_1$ transition. By quantitatively analyzing the relationship between PL intensity and reciprocal temperature through Arrhenius plotting (Fig. 3b), the thermal activation energy was determined by using the following equation:[43]

$$I(T) = \frac{I_0}{1 + A\exp(-E_a/k_bT)} \tag{1}$$

where $I_{(T)}$ and $I_{(0)}$ are the integrated PL intensity at measurement temperature T and 0 K, respectively. A is a pre-exponential factor, E_a represents the thermal activation energy, and k_b is the Boltzmann constant. The derived E_a value for *R*-DACAMnBr$_3$ is 73.2 meV, which substantially exceeds the thermal energy (25 meV) at RT.[44] The relatively large activation energy barrier can effectively suppress non-radiative recombination pathways, thus enhancing the thermal stability and promoting radiative recombination processes.

Further in-depth analysis of the emission FWHM as a function of temperature was carried out to quantify the electron–phonon coupling interactions (Fig. 3c), which is evaluated by using eqn (2):[40]

$$\mathrm{FWHM} = 2.36\sqrt{S}\hbar\omega_{\mathrm{phonon}}\sqrt{\cot h\frac{\hbar\omega_{\mathrm{phonon}}}{2k_{\mathrm{bT}}}} \tag{2}$$

where $\hbar$ is the reduced Planck constant, ω_{phonon} represents the phonon frequency, and T denotes the temperature. The extracted Huang–Rhys factor ($S = 6.04$) and phonon energy ($\hbar\omega_{\mathrm{phonon}} = 35.7$ meV) suggested strong electron–phonon coupling within the crystal lattice.[45] The strong electron–phonon coupling along with the strong crystal field in octahedral coordination endowed the Mn^{2+} emission in *R*-DACAMnBr$_3$ crystals with a large Stokes shift (105 nm). Temperature-dependent PL lifetime measurements were also performed. It was observed that the PL lifetime of *R*-DACAMnBr$_3$ decreased from 1.2 ms at 80 K to 0.97 ms at 300 K (Fig. 3d and e), which is in good agreement with the decline trend of the PL intensity. The k_{nr} values of *R*-DACAMnBr$_3$ at different temperatures from 120 to 300 K were determined based on the corresponding PL lifetimes and PLQYs (Fig. S10 and Table S7†). The results

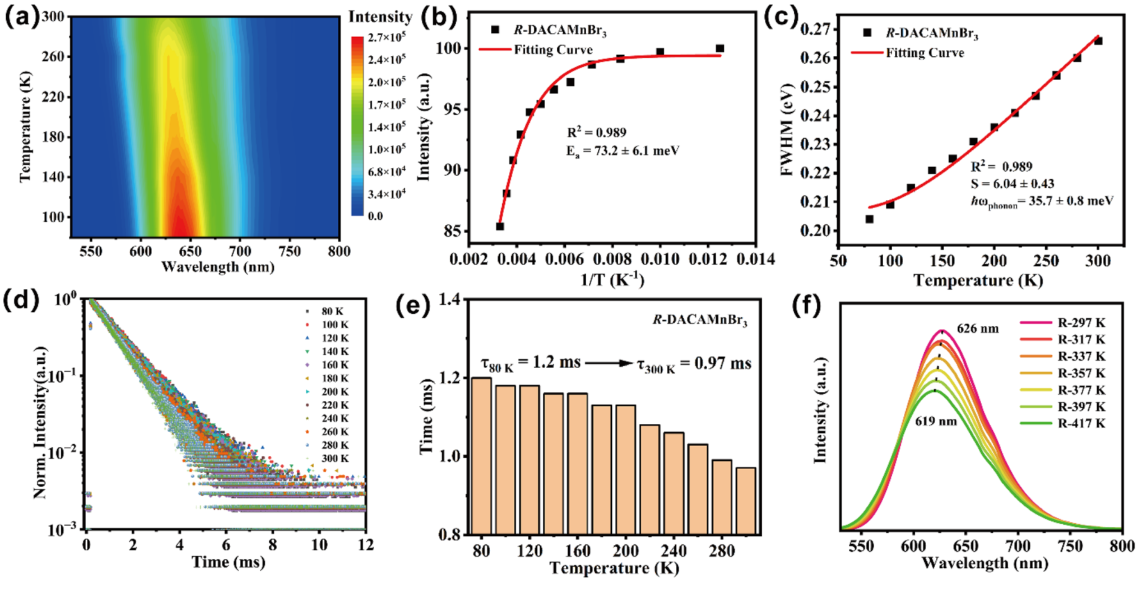

Fig. 3 Temperature-dependent PL properties of *R*-DACAMnBr$_3$. (a) Contour plots of the temperature-dependent PL spectra ($\lambda_{\mathrm{ex}} = 357$ nm) of *R*-DACAMnBr$_3$ in the temperature range of 80–300 K. (b) Integrated PL intensity of *R*-DACAMnBr$_3$ as a function of inverse temperature. (c) FWHM of the Mn^{2+} emission in *R*-DACAMnBr$_3$ as a function of temperature and the fitting to extract the $\hbar\omega_{\mathrm{phonon}}$ and S values. (d) Temperature-dependent PL decay curves ($\lambda_{\mathrm{em}} = 626$ nm) and (e) single exponential fitting results. (f) Temperature-dependent PL spectra ($\lambda_{\mathrm{ex}} = 357$ nm) of *R*-DACAMnBr$_3$ in the temperature range from 297 to 417 K.

showed that as the temperature decreased from 300 to 120 K, the k_{nr} value of the PL emission declined from $7.10 \times 10^2\ \mathrm{s}^{-1}$ to $5.76 \times 10^2\ \mathrm{s}^{-1}$, suggesting a reduction in non-radiative relaxation in *R*-DACAMnBr$_3$ at cryogenic temperatures, thus resulting in enhancement of PL intensity.

Subsequently, the stability of *R*-DACAMnBr$_3$ crystals was evaluated. The XRD pattern, PL spectra and PL lifetime of *R*-DACAMnBr$_3$ crystals stored in a desiccator for 3 months remained essentially unchanged, confirming the good stability of the crystals in dry air (humidity: <30%) (Fig. S11†). Thermogravimetric analysis (TGA) demonstrated that both enantiomers possessed excellent thermal stability, with high decomposition temperature of approximately 270 °C (Fig. S12†). As depicted in Fig. 3f, *R*-DACAMnBr$_3$ crystals were capable of maintaining 88% and 77% of their room-temperature PL intensity when heated to 90 °C and 140 °C, respectively. This clearly indicated their remarkable resistance to thermal quenching, which arose from the effective suppression of non-radiative decay pathways.[46] Moreover, when subjected to continuous UV irradiation at 365 nm for 200 min at temperatures of 25 °C, 90 °C, and 150 °C, *R*-DACAMnBr$_3$ crystals retained more than 95% of their original PL intensity at the corresponding temperature (Fig. S13†). These findings convincingly proved their outstanding thermal stability and photostability.

Chiroptical properties

The chiroptical properties of *R*/*S*-DACAMnBr$_3$ were investigated to elucidate the interplay between their alternating coordination structure and CPL activity. Circular dichroism (CD) spectra revealed mirror-image signals for the enantiomers in the 250–600 nm range (Fig. 4a), with peak positions aligning closely with the Mn^{2+} d–d transition bands observed in UV-vis absorption spectra. Notably, this contrasts with the CD response of the free chiral DACA ligand, which showed mirror symmetry only in the 200–250 nm UV region (Fig. S14†). The pronounced CD activity in the UV-vis range (300–600 nm) directly implicated the inorganic MnOBr$_5$ octahedra as chiral centers, confirming successful chirality transfer from the organic ligand to the Mn^{2+} emitter *via* the alternating coordination architecture. The excited-state chiral activity of *R*/*S*-DACAMnBr$_3$ was probed through CPL spectroscopy. Under a bias of 0.8–0.9 V, the *R*- and *S*-enantiomers exhibited distinct orange CPL signals at 550–800 nm, corresponding to right-handed (negative) and left-handed (positive) circularly polarized emission, respectively (Fig. 4b). The g_{lum} factor, quantifying the degree of CPL asymmetry, is calculated using:[47]

$$g_{\mathrm{lum}} = 2 \times \frac{(I_{\mathrm{L}} - I_{\mathrm{R}})}{(I_{\mathrm{L}} - I_{\mathrm{R}})} \tag{3}$$

where I_{L} and I_{R} represent the intensities of left- and right-handed CPL, respectively. At the emission maximum (626 nm), the g_{lum} values *R*- and *S*-enantiomers were determined to be −0.282 and 0.292, respectively (Fig. 4c), surpassing most chiral OIMHs by 1–3 orders of magnitude. Such exceptional asymmetry originated from the robust chiral coupling between the DACA ligand and Mn^{2+} center, mediated by the direct Mn–O coordination and amplified by the distorted octahedral field. The synergistic effect of coordination and non-covalent interactions in *R*/*S*-DACAMnBr$_3$ ensured minimal chirality loss during the transfer process, a critical advancement over hydrogen-bonded or halogen-mediated systems.

To the best of our knowledge, the g_{lum} values of *R*/*S*-DACAMnBr$_3$ ranked among the highest reported chiral Mn-

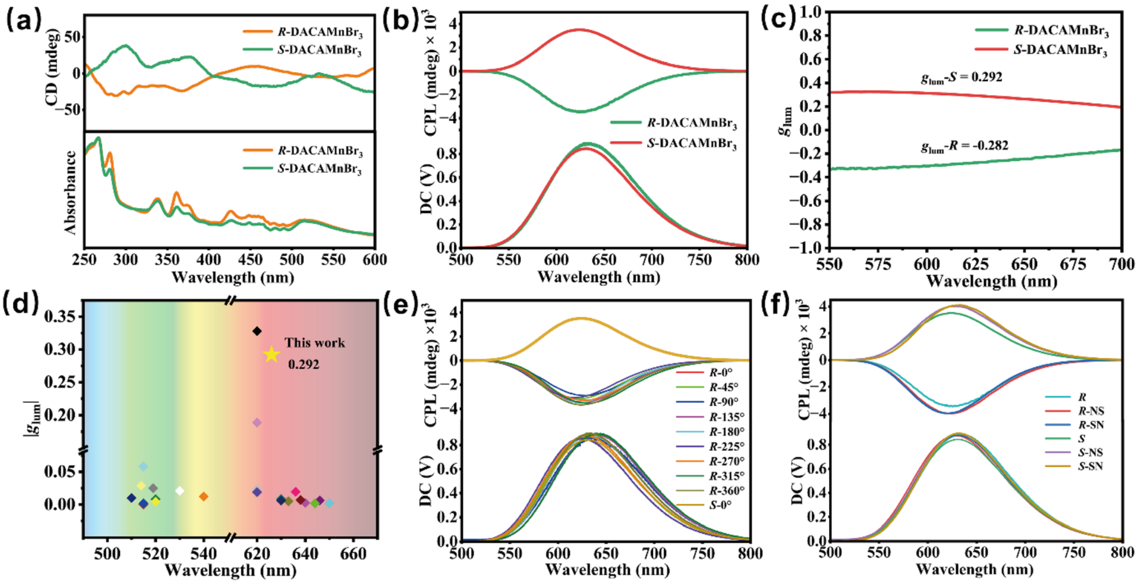

Fig. 4 Chiroptical properties and magnetic response behavior of *R*/*S*-DACAMnBr$_3$. (a) CD and UV-vis absorption spectra of *R*/*S*-DACAMnBr$_3$. (b) CPL emission and (c) g_{lum} spectra ($\lambda_{\mathrm{ex}} = 357$ nm) of *R*/*S*-DACAMnBr$_3$ single crystals. (d) Comparison between the emission wavelengths and the corresponding $|g_{\mathrm{lum}}|$ values of chiral Mn-based OIMHs reported in the literature and this work. (e) CPL spectra of *R*-DACAMnBr$_3$ single crystals with different rotation angles of the crystals. (f) CPL spectra of *R*/*S*-DACAMnBr$_3$ single crystals under an external 1.6 T magnetic field.

based halides (Fig. 4d and Table S8†). This remarkable chiroptical response can be attributed to the unique structural features of these materials. Firstly, rather than relying on the conventional weak hydrogen-bonding forces, the chiral organic ligand is directly coordinated into the inorganic octahedral structure *via* the oxygen atom. This coordination occurs with a shorter interaction distance and stronger interaction force, which is crucial for the chiroptical properties of hybrid OIMHs. Secondly, due to the distinct coordination interaction forces of oxygen and bromine with Mn^{2+}, along with the significant difference in their ionic radii, the octahedron is induced to undergo substantial lattice distortion. This distortion plays a key role in influencing the chiroptical properties. Thirdly, within the octahedral geometry, chiral organic ligands exhibit directionally staggered coordination, leading to the formation of a slightly helical inorganic octahedral 1D chain. These engineered structural features enabled optimized chirality transfer from organic ligands to the inorganic lattice, while coupling with the high emission efficiency of Mn^{2+} to synergistically enhance the generation of a strong CPL signal.

To investigate the influence of structural anisotropy of *R*/*S*-DACAMnBr$_3$ crystals on their CPL properties, we systematically evaluated the CPL performance of *R*/*S*-DACAMnBr$_3$ by rotating the single-crystal sample through 360° at 45° increments.[48,49] As shown in Fig. 4e, the handedness of CPL remained unaltered across all rotation angles, with some fluctuations in g_{lum} from -0.246 to -0.298 (Fig. S15 and Table S9†). The slight variation of g_{lum} values may be attributed to the different thickness and surface morphology of the sample during rotation. Furthermore, CPL measurements were conducted on polycrystalline powder samples of *R*/*S*-DACAMnBr$_3$. The polycrystalline forms displayed pronounced weakening CPL signals, with g_{lum} values reduced by an order of magnitude (-5.2×10^{-2} and 5.7×10^{-2} for *R*- and *S*-polycrystals, respectively; Fig. S16†). Such a significant reduction in chiroptical activity stemmed from the loss of long-range crystallographic order and anisotropic alignment in the polycrystalline state, consistent with prior observations in lead-free chiral OIMHs.[35] These controlled experiments conclusively verified that the robust CPL activity in *R*/*S*-DACAMnBr$_3$ arose from genuine circularly polarized emission governed by the intrinsic chirality of the alternating coordination structure, rather than optical artifacts. The retention of high g_{lum} values in single crystals underscored the critical role of crystal orientation and ordered molecular arrangement within the crystal lattice for achieving high performance CPL materials.

To explore the interplay between chiroptical activity and magnetism, we investigated the magneto-chiroptical coupling effects in *R*/*S*-DACAMnBr$_3$ under an external magnetic field. Hitherto, studies on magnetic-field-modulated CPL in chiral manganese-based halides remain exceptionally rare.[50,51] At room temperature, the CPL responses of both enantiomers were measured under a 1.6 T magnetic field applied parallel (N → S) or antiparallel (S → N) to the excitation light propagation direction (Fig. 4f). Strikingly, the CPL intensity of *R*/*S*-DACAMnBr$_3$ was amplified by the magnetic field, independent of its orientation. The g_{lum} increases by 12.4% (from -0.282 to -0.317) and 9.93% (from 0.292 to 0.321) for the *R*- and *S*-enantiomers, respectively (Fig. S17 and Table S10†). Furthermore, magnetic circular dichroism (MCD) and electron paramagnetic resonance (EPR) were employed to investigate the positive magneto-chiroptical activity of *R*/*S*-DACAMnBr$_3$ crystals (Fig. S18 and S19†). The MCD spectra of *R*/*S*-DACAMnBr$_3$ clearly revealed that the intensities of CD signals noticeably increased when an external magnetic field (1.6 T) was applied, illustrating the enhancement in light absorption of the crystals. The EPR spectrum of *R*-DACAMnBr$_3$ crystals exhibited a single broad peak with a large line width ($\Delta H = 45.1$ mT) instead of six fine-line spectra, indicating that there were strong dipole–dipole interactions between Mn^{2+} ions in R-DACAMnBr$_3$. Therefore, the MCD and EPR results verified that the positive magneto-chiroptical properties were due to the enhanced light absorption and dipole–dipole interactions of *R*/*S*-DACAMnBr$_3$ upon application of an external magnetic field.[52,53] To our knowledge, the positive magneto-chiroptical properties of *R*/*S*-DACAMnBr$_3$ are unprecedented in chiral lead-free OIMHs, which may unlock the potential of coordination-engineered chiral OIMHs as versatile platforms for magneto-chiroptical applications.[54]

Optoelectronic applications

Inspired by the excellent CPL performance, optical and thermal stability, and photophysical properties of *R*/*S*-DACAMnBr$_3$, we fabricated CP-LEDs by integrating *R*-DACAMnBr$_3$ with UV-curing adhesive onto commercial 365 nm UV chips (Fig. 5a). The CP-LEDs emitted a bright and visible orange light with the Commission Internationale de l'Eclairage (CIE) coordinate of (0.62, 0.37) (Fig. 5b and S20†). Systematic characterization of the CP-LEDs under varying operating currents (40–200 mA) revealed excellent color stability and a linear relationship between the emission intensity and driving currents of the crystals (Fig. 5c and S20†). To assess the chiral optical performance, we analyzed the CPL activity of the *R*/*S*-DACAMnBr$_3$-based CP-LEDs by connecting a DC power supply with the device (3.3 V, 0.6 W) (Fig. S21†). We observed that the *R*/*S*-DACAMnBr$_3$-based CP-LEDs show mirror-symmetric CPL signals centered arround 620 nm with g_{lum} values of -5.7×10^{-3} and 6.4×10^{-3}, respectively (Fig. 5d and S22†). The almost unchanged emission intensities of the fabricated CP-LEDs under different cyclic driving currents varying from 30 to 150 mA demonstrated their excellent cycling stability (Fig. 5e). Furthermore, the CP-LEDs retained 80.1% of their original intensity after 3 h of continuous power-on at a constant current of 70 mA (Fig. 5f), indicating their good operational stability. The above findings emphasized the potential of *R*/*S*-DACAMnBr$_3$ as a high-performance, single-component CPL source for advanced optoelectronic applications.

Bulk single crystals with narrow bandgaps, high carrier mobility, and steady-state photocurrent are excellent materials for fabricating efficient optoelectronic devices.[55–58] Over recent years, hybrid Mn-based halides have demonstrated significant potential in X-ray scintillators, spintronics, and LEDs, while their application in photodetection remains largely unexplored. On this basis, we integrated UV photodetectors using large-

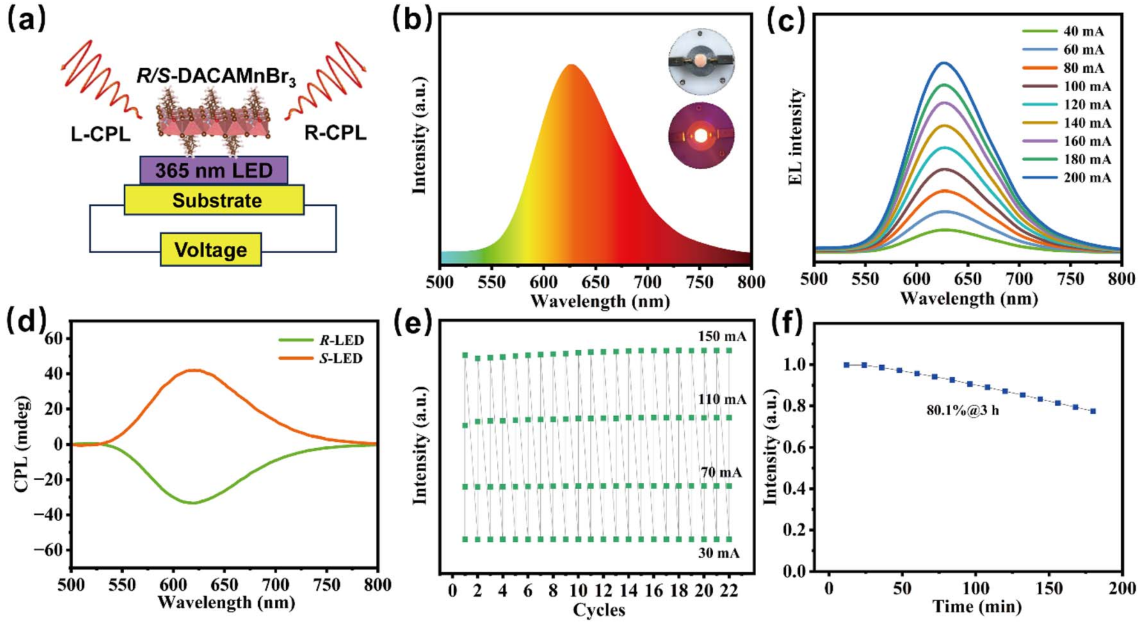

Fig. 5 Optoelectronic applications of R/S-DACAMnBr$_3$. (a) Schematic diagram of the CP-LEDs based on R/S-DACAMnBr$_3$. (b) Emission spectrum of the CP-LED chips coated with R-DACAMnBr$_3$ crystals under working conditions (inset: the photographs of the CP-LEDs under daylight and working conditions). (c) Emission spectra of the CP-LEDs under different driving currents. (d) CPL spectra of the fabricated CP-LEDs. (e) Integrated PL intensities of R-DACAMnBr$_3$-based CP-LEDs recorded at 30, 70, 110 and 150 mA over a span of more than 20 cycles. (f) Time-dependent variation of emission intensity for R-DACAMnBr$_3$-based CP-LEDs during continuous operation at a constant current of 70 mA for 3 h.

sized R-DACAMnBr$_3$ single crystals with silver electrodes (Figs. S23 and S24a†). Under 266 nm laser excitation with biases from −5 V to 5 V, the device exhibited pronounced photoresponse, as evidenced by the current–voltage (I–V) curves measured under both illuminated and dark conditions. The photodetector illustrated an on/off ratio of 7.72 with symmetric I–V characteristics (Fig. S24b†). We also investigated the linear dynamic range and detectivity of the R-DACAMnBr$_3$-based photodetector (Fig. S24c and d†), which manifested the photocurrent density associated with the light power intensity, showing linear dependence with a linear dynamic range (LDR) of 30.82 dB and a specific detectivity of 6.19×10^8 Jones. Furthermore, the fabricated photodetector exhibited good reproducibility over multiple switching cycles (Fig. S24e†). Overall, exploring its potential in photodetectors is conducive to broadening the application scope of chiral manganese-based halides in optoelectronics.

Conclusions

In summary, we have successfully designed and synthesized a unique enantiomeric chiral hybrid manganese bromide, R/S-DACAMnBr$_3$, featuring an infinite 1D chain structure constructed from edge-sharing MnOBr$_5$ octahedra alternately coordinated by chiral DACA ligands. This distinct alternating coordination architecture established a direct and efficient chiral transfer pathway from organic ligands to Mn^{2+} emission centers, synergizing with the intrinsic high PLQY of Mn^{2+} to realize intense orange CPL at 626 nm. The resulting g_{lum} reaches 0.292 for S-DACAMnBr$_3$, surpassing most reported chiral OIMHs by 1–3 orders of magnitude. Remarkably, positive magneto-chiroptical effect under a 1.6 T magnetic field further amplified the g_{lum} value to 0.321 at RT, marking the first demonstration of magnetic-field-enhanced CPL in lead-free OIMHs and highlighting their potential for spintronic applications. The exceptional stability of R/S-DACAMnBr$_3$ has been evidenced by its resistance to thermal quenching (77% emission intensity retention at 140 °C) and UV irradiation (more than 95% intensity retention after 200 minutes at $\lambda_{\mathrm{ex}} = 365$ nm), suggesting its robustness for practical optoelectronic deployment. S-DACAMnBr$_3$-based CP-LEDs displayed stable orange emission with a g_{lum} value up to 6.4×10^{-3}, while single-crystal photodetectors possessed a switching ratio of 7.72. These findings not only advance the rational design of high-performance CPL materials but also open new avenues for developing chiral optoelectronic systems with tailored functionalities toward next-generation 3D displays, spin-based optoelectronics, and magneto-chiroptical devices.

Data availability

The data supporting this article have been included as part of the ESI.†

Author contributions

X. Li and X. Chen conceived the project and revised the manuscript. F. Wang performed the research and wrote the manuscript. T. Chen and L. Wang helped with the CD and CPL spectra measurements and analyses. C. Li, W. Zhang, and W.

Yuan helped with the PL spectra measurements. S. Lu and L. Li helped with the design of the experiments and data analyses. All authors contributed to the general discussion and analysis of the manuscript.

Conflicts of interest

The authors declare that they have no known competing financial interests or personal relationships that could have appeared to influence the work reported in this paper.

Acknowledgements

This work was supported by the National Natural Science Foundation of China (No. 22135008, 22175179, U22A20398, 12174392), and the Self-deployment Project Research Program of Haixi Institutes, Chinese Academy of Sciences (No. CXZX-2022-GH10, CXZX-2022-GS01).

Notes and references

1 K.-H. Jin, Y. Zhang, K.-J. Li, M.-E. Sun, X.-Y. Dong, Q.-L. Wang and S.-Q. Zang, *Angew. Chem., Int. Ed.*, 2022, **61**, e202205317.
2 F. Zinna, M. Pasini, F. Galeotti, C. Botta, L. Di Bari and U. Giovanella, *Adv. Funct. Mater.*, 2017, **27**, 1603719.
3 F. Zinna, U. Giovanella and L. Di Bari, *Adv. Mater.*, 2015, **27**, 1791–1795.
4 L. Wan, J. Wade, X. Shi, S. Xu, M. J. Fuchter and A. J. Campbell, *ACS Appl. Mater.*, 2020, **12**, 39471–39478.
5 D.-W. Zhang, M. Li and C.-F. Chen, *Chem. Soc. Rev.*, 2020, **49**, 1331–1343.
6 J. Han, S. Guo, H. Lu, S. Liu, Q. Zhao and W. Huang, *Adv. Opt. Mater.*, 2018, **6**, 1800538.
7 J. Wang, C. Fang, J. Ma, S. Wang, L. Jin, W. Li and D. Li, *ACS Nano*, 2019, **13**, 9473–9481.
8 J. Ma, C. Fang, C. Chen, L. Jin, J. Wang, S. Wang, J. Tang and D. Li, *ACS Nano*, 2019, **13**, 3659–3665.
9 Y. Zhang, S. Yu, B. Han, Y. Zhou, X. Zhang, X. Gao and Z. Tang, *Matter*, 2022, **5**, 837–875.
10 C. Zhang, S. Li, X.-Y. Dong and S.-Q. Zang, *Aggregate*, 2021, **2**, e48.
11 J. Hu, X. Wen, D. Yang, Y. Chen, Z. Liu and D. Li, *Nano Lett.*, 2024, **24**, 1001–1008.
12 Y. Guo, Y. Xue, C. Geng and C. Li, *Mater. Today Commun.*, 2022, **33**, 104524.
13 J.-Y. Wang, Y. Si, X.-M. Luo, Z.-Y. Wang, X.-Y. Dong, P. Luo, C. Zhang, C. Duan and S.-Q. Zang, *Adv. Sci.*, 2023, **10**, 2207660.
14 M. Deng, N. F. M. Mukthar, N. D. Schley and G. Ung, *Angew. Chem., Int. Ed.*, 2020, **59**, 1228–1231.
15 C.-M. Shi, H. Lu, J.-Y. Wang, G. Long, L.-J. Xu and Z.-N. Chen, *Nat. Commun.*, 2025, **16**, 1505.
16 Y. Wu, M. Li, Z.-g. Zheng, Z.-Q. Yu and W.-H. Zhu, *J. Am. Chem. Soc.*, 2023, **145**, 12951–12966.
17 X.-H. Zhao, X. Hu, M.-E. Sun, X.-M. Luo, C. Zhang, G.-S. Chen, X.-Y. Dong and S.-Q. Zang, *J. Mater. Chem. C*, 2022, **10**, 3440–3446.
18 S. Feng, Y. Ma, S. Wang, S. Gao, Q. Huang, H. Zhen, D. Yan, Q. Ling and Z. Lin, *Angew. Chem., Int. Ed.*, 2022, **61**, e202116511.
19 X.-Y. Luo and M. Pan, *Coord. Chem. Rev.*, 2022, **468**, 214640.
20 W. Zhang, W. Zheng, L. Li, P. Huang, J. Xu, W. Zhang, Z. Shao and X. Chen, *Adv. Mater.*, 2024, **36**, 2408777.
21 Z. Zhou, H. Meng, F. Li, T. Jiang, Y. Yang, S. Liu and Q. Zhao, *Inorg. Chem.*, 2023, **62**, 5729–5736.
22 Y. Qin, P. She, X. Huang, W. Huang and Q. Zhao, *Coord. Chem. Rev.*, 2020, **416**, 213331.
23 D. Liang, H. Xiao, W. Cai, S. Lu, S. Zhao, Z. Zang and L. Xie, *Adv. Opt. Mater.*, 2023, **11**, 2202997.
24 Z.-L. He, J.-H. Wei, J.-B. Luo, Z.-Z. Zhang and D.-B. Kuang, *J. Mater. Chem. C*, 2023, **11**, 1251–1257.
25 K. Taniguchi, P.-J. Huang, S. Kimura and H. Miyasaka, *Dalton Trans.*, 2022, **51**, 17030–17034.
26 Y. Zhang, W.-Q. Liao, D.-W. Fu, H.-Y. Ye, C.-M. Liu, Z.-N. Chen and R.-G. Xiong, *Adv. Mater.*, 2015, **27**, 3942–3946.
27 A. Sen, D. Swain, T. N. G. Row and A. Sundaresan, *J. Mater. Chem. C*, 2019, **7**, 4838–4845.
28 Y. Nagata and T. Mori, *Front. Chem.*, 2020, **8**, 448.
29 Z. Song, X. Liu, C. Yang, Q. Wu, X. Guo, G. Liu, Y. Wei, L. Meng and Y. Dang, *Adv. Opt. Mater.*, 2024, **12**, 2301272.
30 J. Son, G. Jang, S. Ma, H. Lee, C. U. Lee, S. Yang, J. Lee, S. Moon, W. Jeong, J. H. Park, J. Kim, D. H. Kim, J.-S. Park and J. Moon, *Adv. Funct. Mater.*, 2025, **35**, 2413041.
31 Y. Liu, Y. Wei, Z. Luo, B. Xu, M. He, P. Hong, C. Li and Z. Quan, *Chem. Sci.*, 2024, **15**, 15480–15488.
32 Y. Liu, Z. Luo, Y. Wei, C. Li, Y. Chen, X. He, X. Chang and Z. Quan, *Angew. Chem., Int. Ed.*, 2023, **62**, e202306821.
33 C. Li, Y. Wei, Y. Li, Z. Luo, Y. Liu, M. He, Y. Zhang, X. He, X. Chang and Z. Quan, *Small*, 2024, **20**, 2400338.
34 J.-T. Lin, D.-G. Chen, L.-S. Yang, T.-C. Lin, Y.-H. Liu, Y.-C. Chao, P.-T. Chou and C.-W. Chiu, *Angew. Chem., Int. Ed.*, 2021, **60**, 21434–21440.
35 J. Chen, S. Zhang, X. Pan, R. Li, S. Ye, A. K. Cheetham and L. Mao, *Angew. Chem., Int. Ed.*, 2022, **61**, e202205906.
36 D. P. Panda, D. Swain, R. Raghunathan and A. Sundaresan, *Chem. Mater.*, 2024, **36**, 5698–5708.
37 S. Zhang, Y. Zhao, J. Zhou, H. Ming, C.-H. Wang, X. Jing, S. Ye and Q. Zhang, *Chem. Eng. J.*, 2021, **421**, 129886.
38 X. Cheng, X. Chang, Y. Lin, L. Lv, L. Cong, Y. Jia, J. Yin, J. Li and B.-B. Cui, *Small*, 2024, **20**, 2307216.
39 H. Xiao, P. Dang, X. Yun, G. Li, Y. Wei, X. Xiao, Y. Zhao, M. S. Molokeev, Z. Cheng and J. Lin, *Angew. Chem., Int. Ed.*, 2021, **60**, 3699–3707.
40 X. Liu, J. Yang, W. Chen, F. Yang, Y. Chen, X. Liang, S. Pan and W. Xiang, *Nano Res.*, 2023, **16**, 5894–5899.
41 W. Zhang, J. Wei, Z. Gong, P. Huang, J. Xu, R. Li, S. Yu, X. Cheng, W. Zheng and X. Chen, *Adv. Sci.*, 2020, **7**, 2002210.
42 C. Li, D. Tu, Y. Liu, L. Wang, M. Yang, Z. Xie, S. Yu, J. Xu and X. Chen, *J. Lumin.*, 2024, **269**, 120513.
43 T. Chang, Y. Dai, Q. Wei, X. Xu, S. Cao, B. Zou, Q. Zhang and R. Zeng, *ACS Appl. Mater.*, 2023, **15**, 5487–5494.
44 Y. Wang, S. Zhang, H. Hou, Y. Yin, B. Zou and R. Zeng, *J. Lumin.*, 2024, **273**, 120674.

45 G. Blasse and B. C. Grabmaier, *Luminescent Materials*, ed. G. Blasse and B. C. Grabmaier, Springer Berlin Heidelberg, Berlin, Heidelberg, 1994, pp. 33–70.

46 W. Zhang, P. Sui, W. Zheng, L. Li, S. Wang, P. Huang, W. Zhang, Q. Zhang, Y. Yu and X. Chen, *Angew. Chem., Int. Ed.*, 2023, **62**, e202309230.

47 G. Longhi, E. Castiglioni, J. Koshoubu, G. Mazzeo and S. Abbate, *Chirality*, 2016, **28**, 696–707.

48 C. Yang, S. Xiao, H. Xiao, L. Xu and Z. Chen, *ACS Nano*, 2023, **17**, 7830–7836.

49 D.-H. Kong, Y. Wu, C.-M. Shi, H. Zeng, L.-J. Xu and Z.-N. Chen, *Chem. Sci.*, 2024, **15**, 16698–16704.

50 H. Lu, F. Qi, H. Wang, T. He, B. Sun, X. Gao, A. H. Comstock, S. Gull, Y. Zhang, T. Qiao, T. Shao, Y.-X. Zheng, D. Sun, Y. Chen, H.-L. Zhang, Z. Tang and G. Long, *Angew. Chem., Int. Ed.*, 2024, **64**, e202415363.

51 M. P. P. Davydova, L. Meng, M. I. I. Rakhmanova, Z. Jia, A. S. S. Berezin, I. Y. Bagryanskaya, Q. Lin, H. Meng and A. V. V. Artem'ev, *Adv. Mater.*, 2023, **35**, 2303611.

52 S. Sutariya, M. Bsatee, O. Gololobova, D. Diaz-Diestra, B. Thapa, B. R. Weiner, G. Morell, W. M. Jadwisienczak and J. Beltran-Huarac, *ACS Omega*, 2021, **6**, 7598–7604.

53 I. Sarkar, M. K. Sanyal, S. Takeyama, S. Kar, H. Hirayama, H. Mino, F. Komori and S. Biswas, *Phys. Rev. B:Condens. Matter Mater. Phys.*, 2009, **79**, 054410.

54 Z. Shang, T. Liu, Q. Yang, S. Cui, K. Xu, Y. Zhang, J. Deng, T. Zhai and X. Wang, *Small*, 2022, **18**, 2203015.

55 V.-H. Vuong, S. V. N. Pammi, S. Ippili, V. Jella, T. N. Thi, K. S. Pasupuleti, M.-D. Kim, M. J. Jeong, J.-R. Jeong, H. S. Chang and S. G. Yoon, *Chem. Eng. J.*, 2023, **458**, 141473.

56 G. Zhou, Z. Liu, M. S. Molokeev, Z. Xiao, Z. Xia and X.-M. Zhang, *J. Mater. Chem. C*, 2021, **9**, 2047–2053.

57 Y. Wu, W. Fan, Z. Gao, Z. Tang, L. Lei, X. Sun, Y. Li, H.-L. Cai and X. Wu, *Nano Energy*, 2020, **77**, 105170.

58 H. Wang, Z. Li, D. Li, P. Chen, L. Pi, X. Zhou and T. Zhai, *Adv. Funct. Mater.*, 2021, **31**, 2103106.